# Surfactant-Mediated Morphology and Photocatalytic Activity of α-Ag₂WO₄ Material

Nadia G. Macedo,[†] Amanda F. Gouveia,[†] Roman A. Roca,[†] Marcelo Assis,[†] Lourdes Gracia,[‡] Juan Andrés,*[,§] Edson R. Leite,[⊥] and Elson Longo[†]

[†]CDMF, LIEC, Federal University of São Carlos, P.O. Box 676, 13565-905 São Carlos, SP, Brazil
[‡]Department of Physical Chemistry, University of Valencia, Burjassot 46100, Spain
[§]Department of Analytical and Physical Chemistry, University Jaume I, Castelló 12071, Spain
[⊥]Brazilian Nanotechnology National Laboratory (LNNano), Brazilian Center for Research in Energy and Materials (CNPEM), 13083-970 Campinas, SP, Brazil

Ⓢ Supporting Information

**ABSTRACT:** In the present work, the morphology (hexagonal rod-like vs cuboid-like) of an α-Ag₂WO₄ solid-state material is manipulated by a simple controlled-precipitation method, with and without the presence of the anionic surfactant sodium dodecyl sulfate (SDS), respectively, over short reaction times. Characterization techniques, such as X-ray diffraction analysis, Rietveld refinement analysis, Fourier-transform (FT) infrared spectroscopy, FT Raman spectroscopy, UV–vis spectroscopy, transmission electron microscopy (TEM), high-resolution TEM, selected area electron diffraction, energy-dispersive X-ray spectroscopy, field emission-scanning electron microscopy (FE-SEM),



and photoluminescence emission, are employed to disclose the structural and electronic properties of the α-Ag₂WO₄ material. First-principles calculations were performed to (i) obtain the relative stability of the six low-index surfaces of α-Ag₂WO₄; (ii) rationalize the crystal morphologies observed in FE-SEM images (using the Wulff construction); and (iii) determine the energy profiles associated with the transformation process between both morphologies induced by the presence of SDS. Finally, we demonstrate a relationship between morphology and photocatalytic activity, evaluated by photodegradation of Rhodamine B dye under UV light, based on the different numbers of unsaturated superficial Ag and W cations (local coordination, i.e., clusters) of each surface.
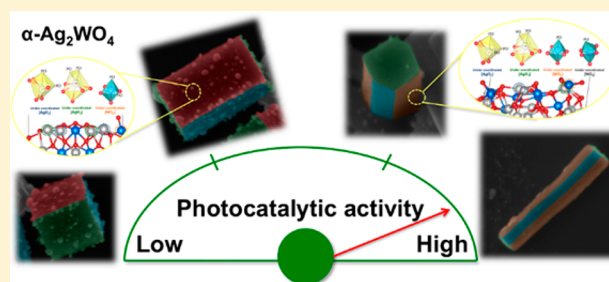
## 1. INTRODUCTION

Organic chemicals are still largely employed by the textile industries and play a critical role in the pollution of river water, causing chemical and biological changes in aquatic systems, which can kill animals and plants.[1] This problem makes the improvement and elucidation of processes like the gas sensing[2] capabilities and photocatalytic degradation of these dyes a priority.[3] Ag₂WO₄ appears to be a good alternative to the extensively researched materials currently used as photocatalysts (e.g., TiO₂,[4] ZnO,[5] WO₃[6]) and should thus be further studied and understood. Recent research reported the photocatalytic activity of α-[7] and β-[8] Ag₂WO₄ under UV light.[9] Orthorhombic α-Ag₂WO₄,[10] which also presents good luminescent,[11] antimicrobial,[12] and gas-sensing[13] properties, offers new opportunities to further optimize the facet-dependent photocatalytic performance of semiconductors.

The structure of α-Ag₂WO₄ was resolved by our research group.[14] It is composed of octahedral [WO₆] and [AgO_n]

clusters ($n = 7$, deltahedral [AgO₇]; $n = 6$, octahedral [AgO₆]; $n = 4$, tetrahedral [AgO₄] and $n = 2$, angular [AgO₂]), as depicted in Figure 1. Because of the particular orthorhombic geometry, structural and electronic distortions and the corresponding variations in Ag–O and W–O bond lengths and O–W–O and O–Ag–O bond angles may be sensed.[15] The properties of this semiconductor change according to the crystallographic phase, size, and morphology, and these variables are all dependent on the synthesis procedure. Each surface of a crystal can possess a particular surface energy, atomic distribution, local coordination (clusters) of exposed metals, vacancies, etc. These results tend to confirm the hypothesis that the properties observed for this material result from a compromise between the presence of local defects (short-range disorder) and crystal lattice ordering
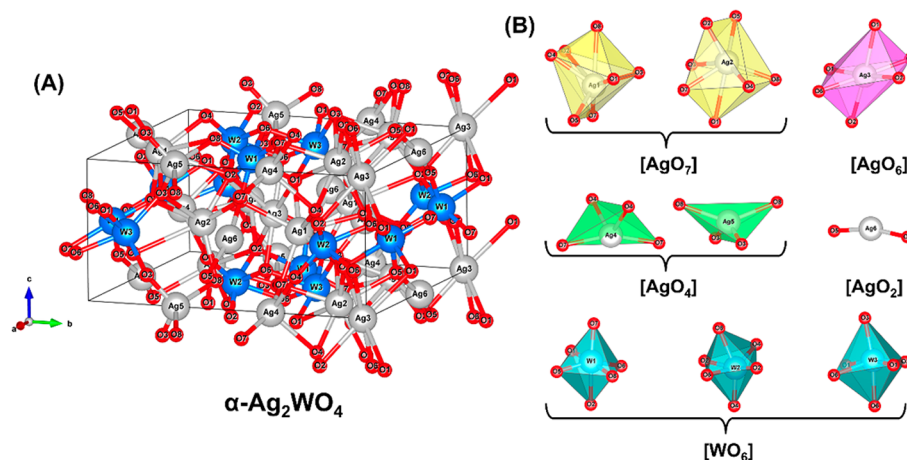
**Figure 1.** (A) The crystal structure of orthorhombic $\alpha$-Ag$_2$WO$_4$ with the space group $Pn2n$ and (B) the different clusters of Ag and W atoms that compose the structure.

(long-range order). Therefore, finding a synthesis method to control these characteristics is crucial to determine the properties and subsequent technological applications of this material.

$\alpha$-Ag$_2$WO$_4$ materials, at nano- and microscale, can be obtained by traditional synthesis methods,[16] or, more recently, by conventional hydrothermal (CH)[17] and microwave hydrothermal (MH)[18] methods. However, there are limitations related to these methods, such as the difficulties of large-scale reproduction, the necessity of specific equipment, the small quantities of product obtained, and safety concerns. Therefore, achieving precise control over the synthesis, morphology, and properties of $\alpha$-Ag$_2$WO$_4$ has become a hot research subject. In this context, controlled-precipitation (CP)[19] is a simple and facile method that is widely employed in the production of $\alpha$-Ag$_2$WO$_4$, which has good bactericide properties and photocatalytic activity. By varying some synthetic parameters of the CP method, such as temperature, stirring time, solvents, or use of capping agents,[20] one can obtain significant changes in the morphology and size of the final samples and, consequently, in some highly surface-dependent properties like photocatalytic activity.[7]

The properties of nanoscale materials and the changes in these properties along with size or shape is a hot research field.[21] Unraveling the relationship between the atomic structure and the functional properties can be a crucial step, especially in complex materials, where short-range interactions, rather than the average structure, can define the actual properties and behavior of the material. One of the main factors determining functionality is the crystal morphology, because the number of active sites is clearly surface-dependent. The variation of reaction conditions can produce different morphologies and, consequently, modify their properties dramatically. However, the control of a crystal morphology is a complex process depending on several factors. Surfactants are particularly important due to their influence on the (nano) particle structure and other physical and chemical properties, having the remarkable ability to control crystal growth and direct it in a morphology- and size-controlled manner.[22] Achieving a detailed understanding of mechanisms by which surfactants can control the morphology of as-synthesized material is of paramount importance, given the effects on the photocatalytic activity of the material.

In this study, we seek to fulfill a threefold objective. The first is to report the novel formation of $\alpha$-Ag$_2$WO$_4$ by a simple CP method, with short reaction time, with and without the presence of an anionic surfactant (sodium dodecyl sulfate, SDS), to evaluate the influence of this surfactant on crystal formation and the resultant structure and morphology. Second, the photocatalytic degradation of Rhodamine B (RhB) will be investigated as a function of the obtained morphology. The third aim is to determine the relationship between morphology and photocatalytic activity.

This paper is organized as follows: Section 2 presents the experimental procedures and computational methods; Section 3 contains the results and discussion; and, finally, Section 4 provides a summary of conclusions.

## 2. METHODS

**2.1. Synthesis.** The $\alpha$-Ag$_2$WO$_4$ crystals were prepared by a simple CP method at 90 °C in the presence of the anionic SDS (C$_{12}$H$_{25}$SO$_4$Na; 90% purity, Synth) as follows: $1 \times 10^{-3}$ mol of dihydrate sodium tungstate (Na$_2$WO$_4$·2H$_2$O; 99% purity, Sigma-Aldrich;) and $2 \times 10^{-3}$ mol of silver nitrate (AgNO$_3$; 98.80% purity, Cennabras) were dissolved separately in 50 mL of deionized water each. SDS (1 g) was added to the sodium tungstate solution, and the solutions were heated under continuous stirring. After the two solutions reached 90 °C, the silver nitrate solution was poured into the sodium tungstate solution and allowed to stir for 5 min. The precipitate was then decanted and washed several times with distilled water. Washing of the precipitate was necessary to eliminate the Na$^+$, NO$^{3-}$, or SO$_4^{2-}$ ions and residual organic compounds. Finally, the precipitate was dried with acetone at room temperature and collected after an overnight period. The reaction was also performed under the same conditions but without the presence of SDS. The precipitates obtained from the reaction without and with SDS are light beige and light brown, respectively.

**2.2. Characterization.** The $\alpha$-Ag$_2$WO$_4$ crystals were structurally characterized by X-ray diffraction (XRD) using a D/Max-2500PC diffractometer (Rigaku, Japan) with Cu K$\alpha$ radiation ($\lambda = 1.5406$ Å) in the $2\theta$ range from 5° to 75°, with a scanning velocity of 2° min$^{-1}$, in the normal routine, and from 10° to 110° with a scanning velocity of 1°/min in the Rietveld routine. The shapes and sizes of the products obtained were observed with a field-emission scanning electron microscope

(FE-SEM), operated at 5−10 kV (Supra 35-VP, Carl Zeiss, Germany). Transmission electron microscopy (TEM) analysis was performed to verify additional morphology details inside a Jeol JEM 2100F with a field emission gun (FEG) operating at 200 kV. Some crystallographic aspects of the samples were also verified with selected area electron diffraction (SAED) analysis and high-resolution transmission electron microscopy (HR-TEM) in the same equipment. Additionally, energy dispersive X-ray spectroscopy (EDS) was also employed to obtain a local elementary composition with EDAX equipment. To verify the complete elimination of the surfactant, thermogravimetric analysis (TGA) was performed with a NETZSCH TG 209 F1 instrument, within the temperature range from 22 to 900 °C, and with a rate of 10k/min, under an atmosphere of synthetic air. Fourier-transform infrared (FT-IR) spectroscopy was performed in a Bomem-Michelson spectrophotometer in transmittance mode (model MB102), in the range from 250 to 1000 cm$^{-1}$, using KBr pellets as a reference. Raman spectra were recorded using the iHR550 spectrometer Horiba Jobin-Yvon coupled to a CCD detector and an argon-ion laser (Melles Griot) operating at 514.5 nm with a maximum power of 200 mW and a fiber microscope. UV−Vis diffuse reflectance measurements were obtained using a Varian Cary spectrometer model 5G on the diffuse reflectance mode, with a wavelength range from 200 to 800 nm, and a scan speed of 600 nm min$^{-1}$. Photoluminescence (PL) measurements were obtained at room temperature with a monochromator (Thermal Jarrel-Ash Monospect-27) linked to a photomultiplier model R446 (Hamatsu Photonics) and a double monochromator (Jobin-Yvon-U1000) directly linked to a system of photon counting. A Krypton laser (Coherent Innova 90k) with a wavelength of 350 nm was used as the excitation source, with a maximum exit power rate of 500 mW. After the passage of the laser beam through the optical chopper, the power was reduced and maintained at 40 mW on the samples. In addition, the surface areas of the samples were obtained by physiosorption of $N_2$ at 77 K in a Micromeritics equipment (ASAP 2420). Before the analysis the samples were heated to 120 °C for 10 h under vacuum to eliminate water and physically adsorbed. The surface area was calculated with the Brunauer−Emmet−Teller (BET) equation.[23]

**2.3. Photocatalysis Assays.** To perform the photocatalysis experiments, 50 mL of RhB (95%, Mallinckrodt) solution (1 × 10$^{-5}$ mol L$^{-1}$) with a pH of 4.0 was mixed with 50 mg of α-$Ag_2WO_4$. The mixture, consisting of the dye and photocatalyst, was irradiated in a dark box using six UV lamps (Phillips TL-D, 15 W). Before UV illumination, the suspensions were sonicated for 10 min in an ultrasonic bath (42 kHz, model 1510) to allow saturated absorption of RhB onto the catalyst. Subsequently, the dispersion containing the catalyst and the dye was transferred to a vessel inside the photoreactor, with the temperature maintained at 20 °C via a thermostatic bath and vigorous stirring. At 0, 5, 10, 20, 30, 50, 70, 90, and 120 min, a 2 mL aliquot of the suspension was removed from the photocatalytic system and placed in a plastic tube, which was centrifuged at 13 000 rpm for 10 min to separate the solid catalyst from the liquid phase. Finally, the kinetics of the dye photodegradation process were monitored in a commercial cuvette via UV−vis spectroscopy (JASCO V-660) at 554 nm. This procedure was subsequently performed for each synthesized α-$Ag_2WO_4$ sample.

**2.4. Computational Details.** From the calculated surface energy ($E_{surf}$) values for the six low-index crystals facets reported by Andrés et al.,[24] it is possible to determine the equilibrium shape and ideal morphology, by using the Wulff construction. Furthermore, by changing the relative surface energy values of each facet, we found a map of available morphologies for α-$Ag_2WO_4$, as well as the pathways linking the ideal and given morphologies, including both hexagonal rod-like and cuboid-like morphologies.[24]

This methodology provides a simple relationship between $E_{surf}$ and the distance of the planes and has been used in materials science to predict experimental crystal shapes.[25]

In this study, we go further by calculating the energy profiles of the paths connecting different morphologies from the values of the polyhedron energy ($E_{polyhedron}$) by a function of the form

$$E_{polyhedron} = \sum_i C_i \times E_{surf}^i \tag{1}$$

where $C_i$ is the percentage contribution of the surface area to the total surface area of the polyhedron, $C_i = A^i/A^{polyhedron}$, and $E_{surf}^i$ is the surface energy of the corresponding surface. The energy profiles were calculated by decreasing and/or increasing the $E_{surf}$ values of a given surface of the polyhedron.

## 3. RESULTS AND DISCUSSION

**3.1. X-ray Diffraction Analysis.** Figure 2 shows the XRD patterns of the synthesized α-$Ag_2WO_4$ crystals. According to
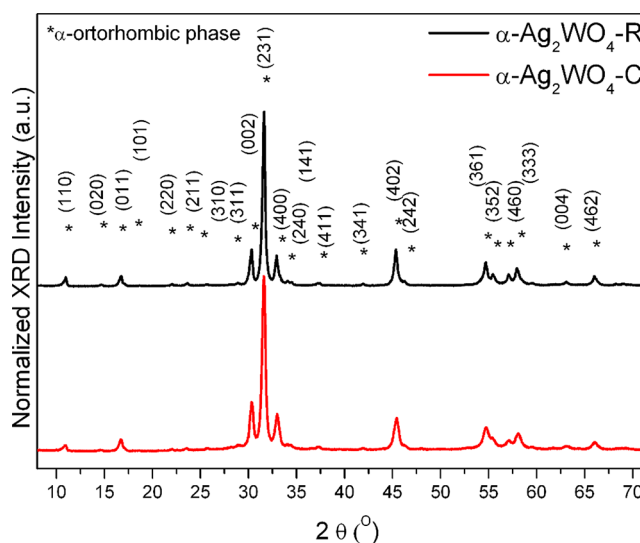
**Figure 2.** Normalized XRD patterns of the α-$Ag_2WO_4$ crystals synthesized by the CP method at 90 °C without (black) and with (red) the presence of anionic surfactant SDS.

the Inorganic Crystal Structure Database, ICSD card 34−61, these crystals have an orthorhombic structure, without any deleterious phases, with the space group $Pn2n$ and point group symmetry ($C_{2v}^{10}$).[26] Therefore, the samples synthesized by the CP method with and without anionic surfactant SDS present a pure α-phase structure. Both crystals have sharp and well-defined diffraction peaks, which indicate a good degree of long-range structural order in the lattice, and they are all in good agreement with the respective databases. There are also no significant variations in peak intensity or position between both samples.

**3.2. Rietveld Refinement Analysis.** The structural refinement using the Rietveld method[27] was performed using GSAS program, version 1. The refinement plots for the α-
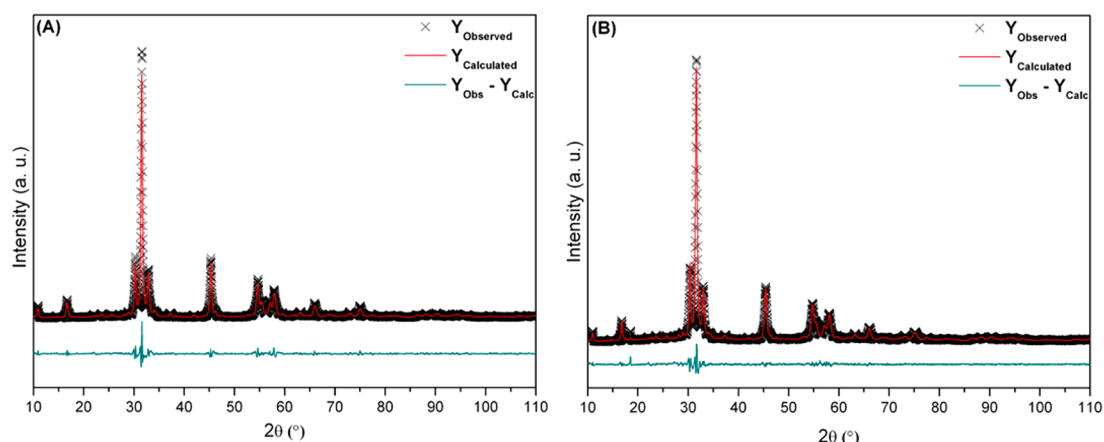
**Figure 3.** Rietveld refinement plots of $\alpha$-Ag$_2$WO$_4$ crystals synthesized by the CP method at 90 °C without (A) and with (B) the presence of anionic surfactant SDS.

Ag$_2$WO$_4$ crystals synthesized by the CP method at 90 °C without and with the presence of SDS, respectively, were depicted in Figure 3A,B. The Rietveld refinement confirms the orthorhombic structure, with only a small variation between the values obtained in the refinement and the literature.[14] The structural results ($a$, $b$, $c$ cell parameters and volume) with the statistical reliability parameters ($R_{wp}$ and GOF) are shown in Table 1. The statistical reliability of the parameters indicates a high agreement between the calculated and observed X-ray patterns for both samples.

**Table 1. Rietveld Refinement Results for $\alpha$-Ag$_2$WO$_4$ Crystals Synthesized by the CP Method at 90 °C without (A) and with (B) the Presence of Anionic Surfactant SDS**

| sample | $a$ (Å) | $b$ (Å) | $c$ (Å) | volume | $R_{wp}$(%) | GOF |
|--------|---------|---------|---------|--------|-------------|-----|
| A | 10.897 | 12.033 | 5.904 | 773.430 | 9.8 | 1.91 |
| B | 10.851 | 12.036 | 5.889 | 769.636 | 7.4 | 1.64 |
| ref[14] | 10.878 | 12.009 | 5.895 | 770.09 | 12.3 | 1.88 |

**3.3. Morphological Analysis.** FE-SEM analysis is a very powerful tool to provide morphological information, such as the arrangement of atoms in the structure and the degree of structural and electronic order/disorder. Figure 4 shows the FE-SEM images of the experimentally obtained products.
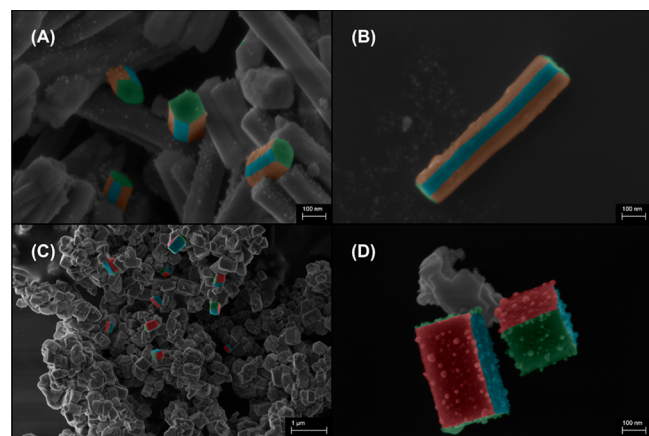


**Figure 4.** FE-SEM images of $\alpha$-Ag$_2$WO$_4$ obtained by the CP method: (A, B) $\alpha$-Ag$_2$WO$_4$-R crystals and (C, D) $\alpha$-Ag$_2$WO$_4$-C crystals.

Figure 4A is an image of $\alpha$-Ag$_2$WO$_4$ crystals obtained from the short period stirring synthesis without surfactant under 90 °C. The observed morphology is hexagonal rod-like, in accordance with previous studies found in literature,[7] and is depicted in Figure 4B. The hexagonal rod-like $\alpha$-Ag$_2$WO$_4$ crystals usually have a length of nearly 2 $\mu$m. In this case, probably due to the short time of stirring (5 min), the crystals are smaller (see Figure 5).

Figure 4C displays the morphology of the product obtained when the anionic surfactant SDS is included in the CP method, maintaining the other conditions constant. It is possible to observe several cuboid-like crystals, depicted in Figure 4D. Although there are some reports in the literature of rectangular nanorod crystals of Ag$_2$WO$_4$ combined with hexagonal rods,[28] this is the first report in which the predominance of cuboid-like morphology is observed. The samples synthesized without and with anionic surfactant SDS are designated, according to their morphology, as $\alpha$-Ag$_2$WO$_4$-R ($\alpha$-Ag$_2$WO$_4$ hexagonal rod-like crystals) and $\alpha$-Ag$_2$WO$_4$-C ($\alpha$-Ag$_2$WO$_4$ cuboid-like crystals), respectively.

The FE-SEM image (Figure 4D) also shows two crystals, one possessing a cubic shape, $\alpha$-Ag$_2$WO$_4$-C, and the other being exactly twice the length of the first one. An analysis of the histogram in Figure 5 renders a length distribution ranging from 100 to 300 nm, in the case of the cuboid crystals, with an average of nearly 200 nm. These results seem to indicate that the basic cubic blocks link to each other by coalescence in such a way that the theoretical cubes become elongated cuboid-like particles.

As studied before by our work group,[15,29] the irradiation of $\alpha$-Ag$_2$WO$_4$ by an electron beam generates the formation of metallic Ag nanoparticles on their surface.[30] Figure 6A,B displays the TEM images of the Ag$_2$WO$_4$-R and $\alpha$-Ag$_2$WO$_4$-C samples, respectively. Figure 6C,D displays the SAED analysis by HR-TEM. The patterns are diffuse halo rings typical from amorphous materials. The presence of these diffuse rings indicates the changes in interatomic spacing induced by the deformation process.[29] The formation of Ag nanoparticles at some regions on the surface $\alpha$-Ag$_2$WO$_4$ are confirmed by HR-TEM analysis as it is shown in Figure 6E,G, as the interplanar distances between (111) planes, 2.35 Å, of the Ag cubic structure, according to ICSD No. 064706. The local elementary analysis EDS shown in Figure 6F,H also confirms the presence
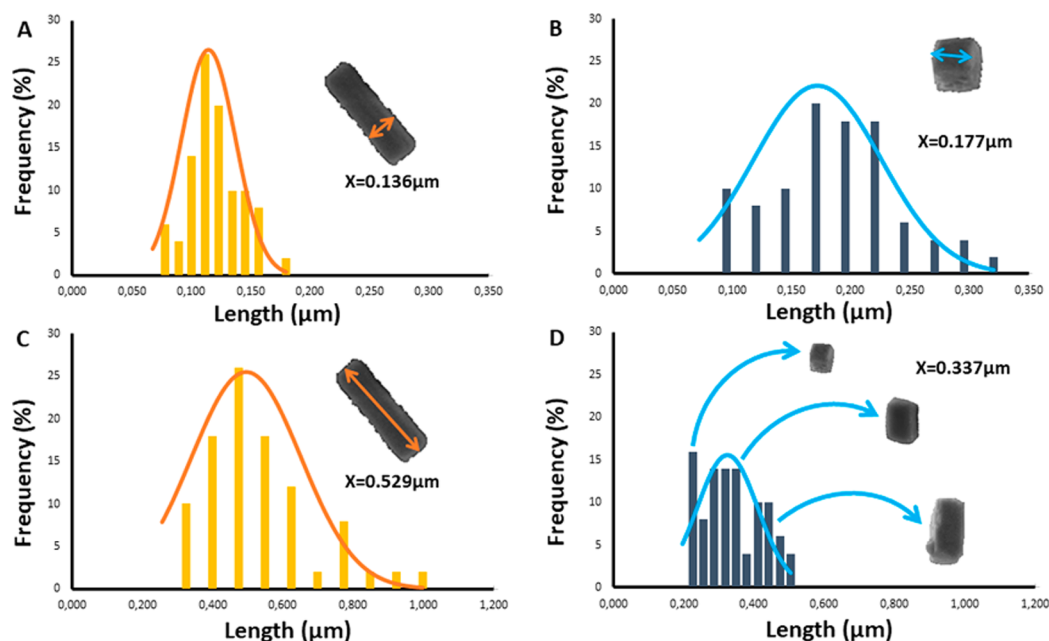
**Figure 5.** Average height and width distribution of $\alpha$-Ag$_2$WO$_4$-R crystals (A, B) and $\alpha$-Ag$_2$WO$_4$-C crystals (C, D).
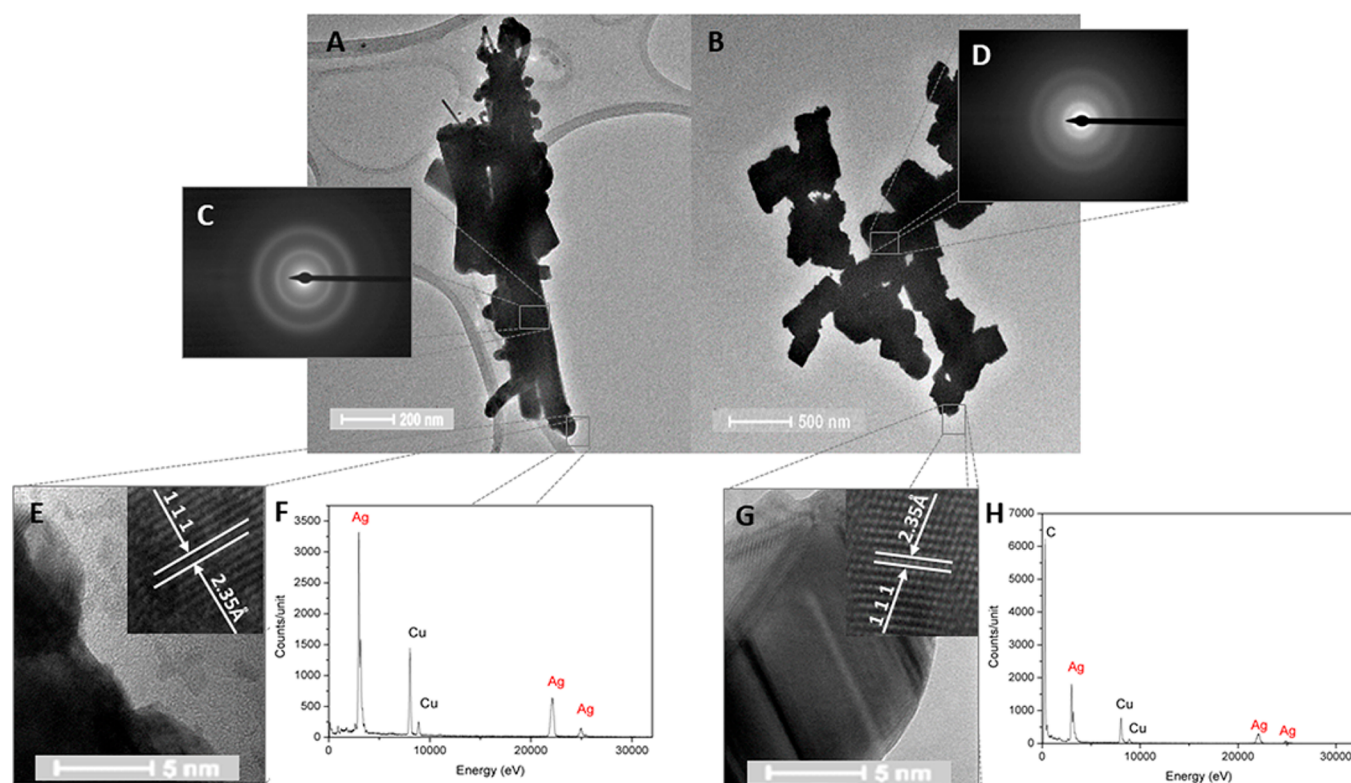


**Figure 6.** TEM images for (A) $\alpha$-Ag$_2$WO$_4$-R and (B) $\alpha$-Ag$_2$WO$_4$-C samples. SAED analysis for (C) $\alpha$-Ag$_2$WO$_4$-R and (D) $\alpha$-Ag$_2$WO$_4$-C samples. HR-TEM images: (E) $\alpha$-Ag$_2$WO$_4$-R and (G) $\alpha$-Ag$_2$WO$_4$-C. EDS local elementary analysis: (F) $\alpha$-Ag$_2$WO$_4$-R and (H) $\alpha$-Ag$_2$WO$_4$-C. (inset, E, G) The calculated interplanar distance corresponding to cubic Ag metal at the $\alpha$-Ag$_2$WO$_4$-R and $\alpha$-Ag$_2$WO$_4$-C samples, respectively.

of metallic Ag, Cu, and C shown in the elementary analysis EDS.

**3.4. FT-IR and FT-Raman Spectroscopies.** Analysis of the FT-IR and FT-Raman data provides information about the local coordination of Ag and W cations that form the crystalline structure. Figure 7A presents the FT-IR spectra for both materials. The intense bands localized at 829 and 860 cm$^{-1}$ for both samples are due to the asymmetric vibrations of the O−

W−O moiety in [WO$_6$] distorted clusters. The bands identified at 320 and 294 cm$^{-1}$ are related to the symmetric vibrations and torsional motions in [WO$_6$] distorted clusters. Present data are in good agreement with previous results reported in the literature.[31]

Figure 7B presents the Raman scattering spectra and the vibrational modes in the range of 50−1200 cm$^{-1}$ at room temperature. Although there are 21 known vibrational modes
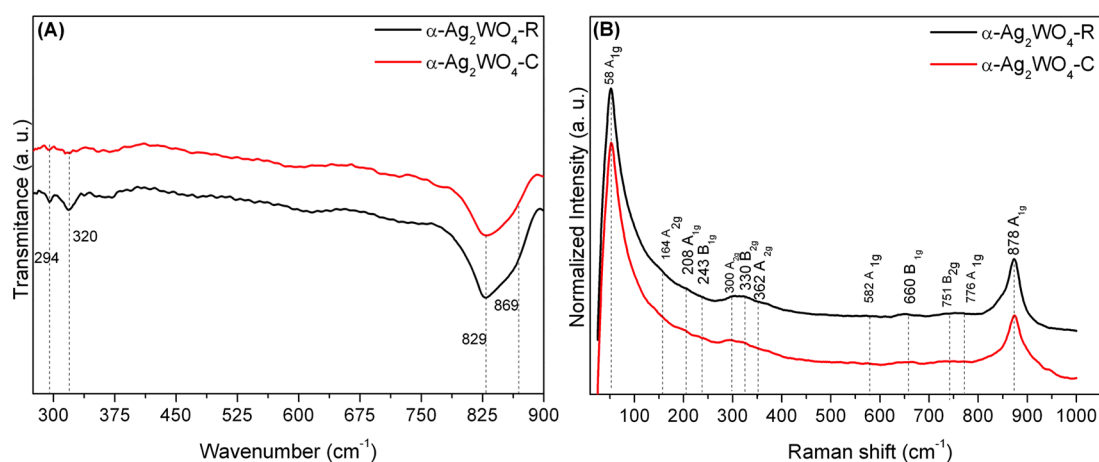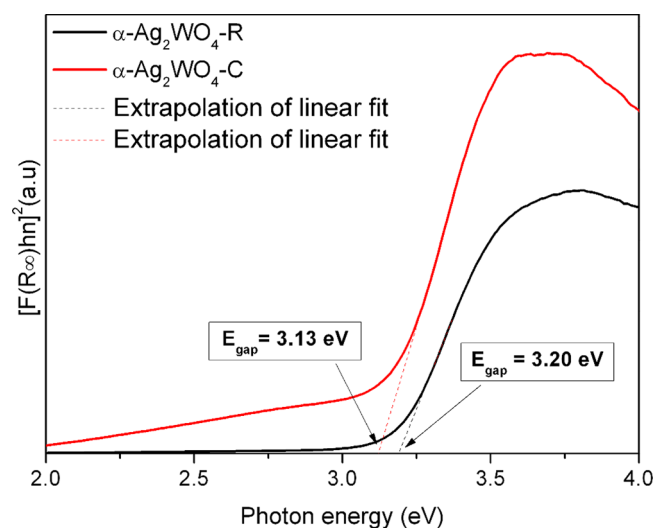
**Figure 7.** (A) FT-IR spectra of $\alpha$-Ag$_2$WO$_4$-R (black) and $\alpha$-Ag$_2$WO$_4$-C (red). (B) Raman spectroscopy of $\alpha$-Ag$_2$WO$_4$-R (black) and $\alpha$-Ag$_2$WO$_4$-C (red). The vertical dashed lines indicate the position of the Raman peaks and active modes.

for $\alpha$-Ag$_2$WO$_4$ (6 A$_{1g}$, 5 A$_{2g}$, 5B$_{1g}$, and 5B$_{2g}$)[32] it is possible to detect 12 of them for both samples. According to Turkovic et al.,[32] there are two active A$_{1g}$ external modes within the region of smaller wavenumbers, at 44 and 60 cm$^{-1}$, that are due to the translational movements of Ag cations in a rigid molecular unit. In our spectra, it is possible to observe, for both materials, an intense band at ~58 cm$^{-1}$. This peak is identical in intensity and definition for both samples. The active modes between 500 to 100 cm$^{-1}$ are related to external vibrational modes of [AgO$_n$] ($n$ = 7, 6, 4, 2).[28] Although this region presents lower-intensity bands, it seems to indicate some slight differences between the spectra. There is an intense band at 878 cm$^{-1}$, attributed to the symmetric stretching of the W–O bond in [WO$_6$] octahedral clusters. The active modes, between 500 and 1000 cm$^{-1}$, can be assigned to the vibrations in [WO$_6$] clusters. This result confirms that the Raman spectra are the result of the presence of short-range order at the [AgO$_n$] clusters within the crystal lattice.

**3.5. UV–Vis Optical Spectroscopy Analysis.** The optical band gap energy ($E_{gap}$) values for both $\alpha$-Ag$_2$WO$_4$ samples were determined by UV–vis spectroscopy. With the utilization of the Wood and Tauc method[33] we could estimate the energy gaps of the materials. The spectra obtained were converted to the Kubelka–Munk function, by the method proposed by Kubelka and Munk-Aussig,[34] which is a reliable method to estimate $E_{gap}$ values with good accuracy within the limits of assumptions in three dimensions. According to Kim et al.[35] and Tang et al.,[36] Ag$_2$WO$_4$ crystals exhibit an optical absorption spectrum governed by direct electronic transitions between the valence band (VB) and conduction band (CB). On the basis of this information, the $E_{gap}$ values of our $\alpha$-Ag$_2$WO$_4$ crystals were calculated using $n$ = 0.5.

UV–Vis spectroscopy provides structural information in terms of the structure of electronic bands and the level of organization at both short and medium ranges. A characteristic behavior of UV–vis absorbance curves is the formation of an exponential decay within the regions of lesser energies known as Urbach Tail.[33] This decay is associated with the presence of an intermediate-energy band gap. The gradient of the linear extrapolation on this "tail" correlates with the amount of disorder in the material: the less steep the linear extrapolation on this tail, the more disordered is the material. Because Ag$_2$WO$_4$ is composed of several different clusters ([WO$_6$], [AgO$_7$], [AgO$_6$], [AgO$_4$], [AgO$_2$]), with weak interactions

between the O–W and O–Ag bonds, the relative positions of the atoms (W, O, Ag) can vary. These variations can affect both bond lengths and angles, which causes a redistribution of the electronic density and the energy band structure, thus changing the band gap value. Reported experimental values are in the range of 3.09 and 3.23 eV,[7,14] depending on the synthesis method employed. We obtained an $E_{gap}$ value of 3.20 eV for the $\alpha$-Ag$_2$WO$_4$-R and 3.13 eV for the $\alpha$-Ag$_2$WO$_4$-C (Figure 8).



**Figure 8.** UV–Vis spectra of $\alpha$-Ag$_2$WO$_4$-R (black) and $\alpha$-Ag$_2$WO$_4$-C (red).

Both values fall within the range of values previously reported. Although the differences in value might be small, it could be related to the individual band gaps of each surface given that the $E_{gap}$ value is the result of bulk and surface contributions. Moreover, one might consider the influence of some possible defects, such as structural distortions, associated with changes in bond lengths and angles, atomic dislocation, local coordination changes, oxygen vacancies, etc.[37]

The presence of such defects is very dependent on the synthesis parameters, such as solvent, time, temperature, pressure, surfactants, or contaminants. From an electronic point of view, these defects generate intermediate energy states in the forbidden region between the VB and CB, while an increase of the $E_{gap}$ values can be attributed to a reduction in

the number of defects and, subsequently, in the number of electronic levels within the forbidden band gap.

**3.6. Photoluminescence Emissions.** PL is an optical property that conveys information about the electronic states and about the level of structural organization in the intermediate range. PL emissions are dependent on the synthesis conditions and on the presence of impurities, distortions and deformations of the clusters, etc.[37] For this reason, PL measurements can be used as a complementary tool to X-ray diffraction and FT-Raman and UV−vis spectroscopies to obtain information about the level of order−disorder and defect density of the material. It can also help to explain the appearance of intermediate states between the VB and CB.

$\alpha$-$Ag_2WO_4$ has PL emission at room temperature with a broadband character.[38] This is typical of materials where the relaxation step occurs in several paths, with the participation of several energy states within the band gap, according to the broadband model. This broadband is generally composed of blue and green light components, which indicates a high level of mainly shallow defects. This emission is attributed to intrinsic transitions of the $[WO_4]^{2-}$ clusters, as well as charge-transfer processes between distorted $[WO_6]$ to undistorted $[WO_6]$ clusters,[39] which generates shallow defects adjacent to the bands.

Figure 9 presents the PL spectra at room temperature. Both samples show PL emissions from 380 to 800 nm. We can
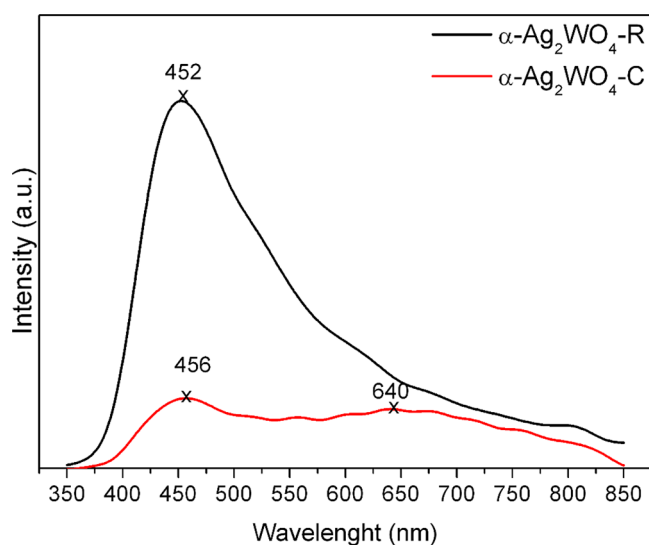


**Figure 9.** PL spectra of $\alpha$-$Ag_2WO_4$-R (black) and $\alpha$-$Ag_2WO_4$-C (red).

observe that the PL behavior of $\alpha$-$Ag_2WO_4$-R presents a broad band with maximum emission at 452 nm, corresponding to the blue region of the electromagnetic spectrum. Though the $\alpha$-$Ag_2WO_4$-C also presents emission in the blue region (456 nm), this band is much less intense, and the curve is much more shifted into the whole spectrum, with emission in the red region (640 nm) with almost the same intensity of the blue emission peak. This behavior can be associated with the decreasing number of distorted $[WO_6]$ clusters and increasing presence of distorted $[AgO_n]$ ($n$ = 7, 6, 4, and 2) clusters, which can be attributed to oxygen vacancies, which induce more disorder to the material and more deep defects in the forbidden region.

**3.7. Morphology Control.** Surface energy does not only dictate the surface structure and stability, but it is also a

fingerprint to measure the catalytic activity and selectivity, as well as to follow the degradation process and the crystallization pathway. The surface energy value provides insight into the resistance of a given material to sintering, ripening, and in dissolution processes. Surface energy is not a constant material property and may depend on the environment that surrounds the surface, such as the adsorption of a reactant, surfactant, or any species present in the solution, which can promote the stability of a particular surface, structure, or facet. Therefore, the control of the crystal morphology is a complex process depending on several factors related to crystal internal structures and external agents. Hence, the synthesis process can have a strong influence on the final product. In our study, when the anionic surfactant SDS is included in the synthesis of $\alpha$-$Ag_2WO_4$, the result indicates that SDS works as a morphology-controlling agent.

It is well-established that, during crystal growth, the shape evolution is controlled by the surface energy of each face. Under equilibrium conditions, faces with high surface energies tend to grow rapidly, so that they usually disappear to minimize the total surface energy.[40] In a given environment, driven by the experimental conditions, the surface energies of different surfaces can be effectively decreased by the selective adsorption of appropriate inorganic or organic agents.[41]

Bakshi[22] showed that the adsorption of a surfactant in aqueous media takes place through bilayer formation. The polar heads of surfactant molecules adhere to the charged nanoparticle surfaces, exposing the organic surfactant tails to the bulk solution, where they are insoluble. A second surfactant layer adsorbs to the first one, making a bilayer. This kind of adsorption is usually selective to a specific crystal plane, which leads to an ordered shape evolution. Hydrophobicity is a very important characteristic in surfactant action and has a strong correlation with the final morphology. The cubic shape is usually generated in the presence of a highly hydrophobic medium.

In this way, the surface plays an important role in the material growth process, and it is fundamental to study the atomic arrangement on each surface. Table 2 presents the surface energy values for each surface.[24] By employing the Wulff construction we can obtain the ideal morphology of $\alpha$-$Ag_2WO_4$, as well as the experimentally observed hexagonal rod-like $\alpha$-$Ag_2WO_4$-R (see Figure 4B) and the cuboid-like $\alpha$-$Ag_2WO_4$-C (see Figure 4D) morphologies. The $E_{surf}$ values show the following stability order: (010) < (100) < (001) < (110) < (101) < (011).

Figure 10 displays the six low-index surfaces of $\alpha$-$Ag_2WO_4$. At the top of each surface, there are different kinds of under-coordinated Ag and/or W cations with respect to the bulk. These local coordinations, associated with incomplete $[AgO_n]$ and $[WO_6]$ clusters, allow us to find the number of broken Ag−O and W−O bonds. Then, the Kröger−Vink notation[42] can be employed to assign the number and type of oxygen vacancies $[V_O^x]$.

An analysis of the results presented in Table 2 and Figure 10 indicates that the most stable surface, (010), presents only one type of under-coordinated cluster $[AgO_4 \cdot 3V_O^x]$ at the Ag1 cation. In the (100) surfaces, Ag1 and Ag2 cations appear under-coordinated with $[AgO_5 \cdot 2V_O^x]$ clusters, and $[WO_4 \cdot 2V_O^x]$ clusters are observed for the W1 cation. In the (001) surface shows the $[AgO_5 \cdot 2V_O^x]$, $[AgO_4 \cdot 3V_O^x]$, and $[AgO_4 \cdot 2V_O^x]$ clusters associated with the Ag1, Ag2, and Ag3 cations, respectively, while there are $[WO_5 \cdot V_O^x]$ clusters at the W1 cation. In the case

**Table 2. Surface Energy Values ($E_{surf}$, eV), Contribution of the Surface Area by the Total Area ($C_i$, %), and the Polyhedron Energy ($E_{polyhedron}$, eV) for Each Morphology of $\alpha$-Ag$_2$WO$_4$**

| surface | $E_{surf}$ ($C_i$) | | |
|---|---|---|---|
| | $\alpha$-Ag$_2$WO$_4$−ideal | $\alpha$-Ag$_2$WO$_4$-R | $\alpha$-Ag$_2$WO$_4$-C |
| **(010)** | 0.20 (52.5) | 0.80 (14.4) | 0.20 (33.3) |
| **(100)** | 0.38 (27.6) | 0.70 (0.00) | 0.20 (33.3) |
| **(001)** | 0.53 (19.9) | 0.20 (35.6) | 0.20 (33.3) |
| **(110)** | 0.65 (0.00) | 1.10 (0.00) | 1.10 (0.00) |
| **(101)** | 0.68 (0.00) | 0.32 (50.0) | 0.68 (0.00) |
| **(011)** | 0.83 (0.00) | 0.83 (0.00) | 0.83 (0.00) |
| $E_{polyhedron}$ | 0.31 | 0.35 | 0.20 |

| surface | $E_{surf}$ ($C_i$) | | | | | | |
|---|---|---|---|---|---|---|---|
| | A | B | C | D | E | F | G |
| **(010)** | 0.20 (45.7) | 0.20 (44.4) | 0.20 (40.3) | 0.50 (18.6) | 0.80 (14.4) | 0.20 (39.6) | 0.20 (42.1) |
| **(100)** | 0.38 (15.0) | 0.70 (0.00) | 0.70 (0.00) | 0.70 (0.00) | 0.70 (0.00) | 0.38 (20.8) | 0.20 (42.1) |
| **(001)** | 0.53 (0.00) | 0.53 (0.00) | 0.20 (24.8) | 0.20 (35.4) | 0.20 (35.6) | 0.20 (39.6) | 0.53 (15.8) |
| **(110)** | 0.65 (0.00) | 0.65 (0.00) | 0.65 (0.00) | 0.65 (6.50) | 1.10 (0.00) | 0.65 (0.00) | 0.65 (0.00) |
| **(101)** | 0.32 (39.3) | 0.32 (55.6) | 0.32 (34.9) | 0.32 (39.5) | 0.32 (50.0) | 0.68 (0.00) | 0.68 (0.00) |
| **(011)** | 0.83 (0.00) | 0.83 (0.00) | 0.83 (0.00) | 0.83 (0.00) | 0.83 (0.00) | 0.83 (0.00) | 0.83 (0.00) |
| $E_{polyhedron}$ | 0.27 | 0.27 | 0.24 | 0.33 | 0.35 | 0.24 | 0.25 |
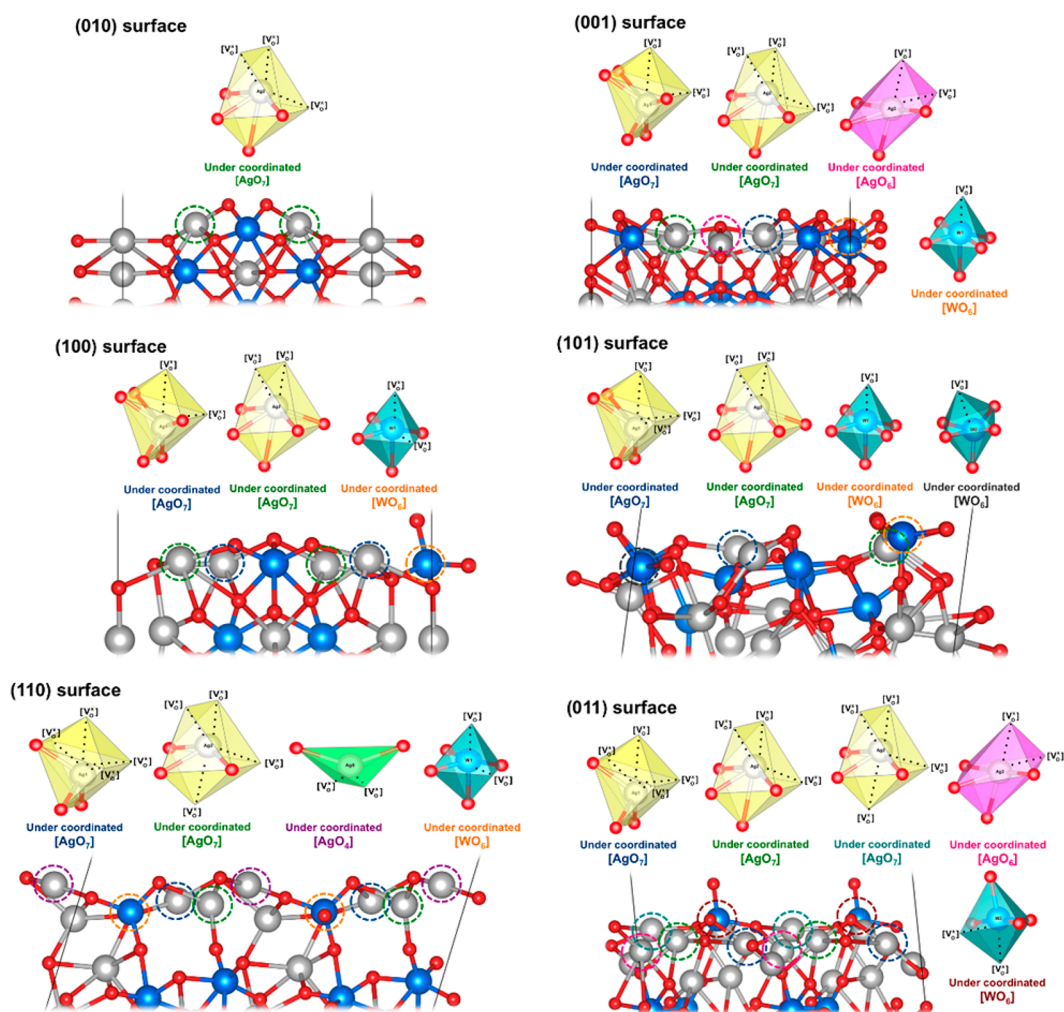


**Figure 10.** Under-coordinated Ag and W clusters at the (010), (001), (100), (101), (110), and (011) surfaces of the $\alpha$-Ag$_2$WO$_4$.

of the (110) surface, $[AgO_4 \cdot 3V_O^x]$ clusters for Ag1 and Ag2 cations, $[AgO_2 \cdot 2V_O^x]$ clusters for the Ag5 cation, and $[WO_4 \cdot 2V_O^x]$ clusters for the W1 cation are found. The (101) surface is

formed by $[AgO_4 \cdot 3V_O^x]$ and $[AgO_5 \cdot 2V_O^x]$ clusters of Ag1 and Ag2 cations, respectively, and $[WO_5 \cdot V_O^x]$ clusters for W1 and W2 cations. At the most unstable surface (011), there are five
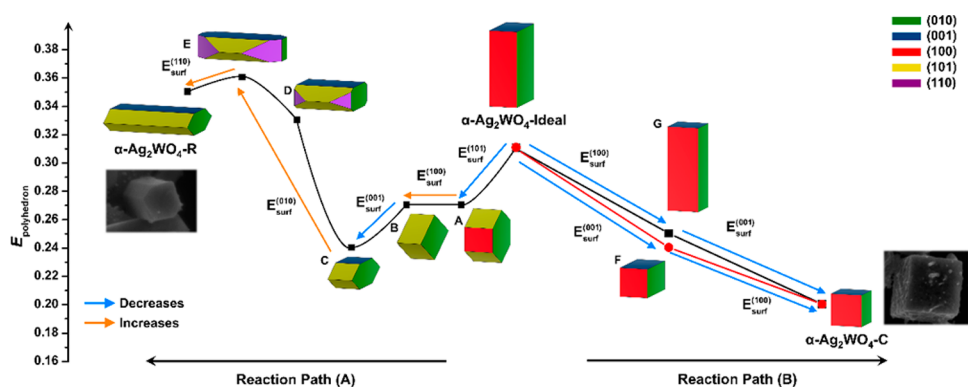
**Figure 11.** Schematic representation of the energy profile to obtain the (A) $\alpha$-Ag$_2$WO$_4$-R and (B) $\alpha$-Ag$_2$WO$_4$-C morphologies. The intermediate morphologies are indicated as A−G, obtained by decreasing/increasing the $E_{surf}$ values involved in the process. Experimental FE-SEM images of $\alpha$-Ag$_2$WO$_4$-R and $\alpha$-Ag$_2$WO$_4$-C morphologies of the studied samples are included for comparison.

different kinds of clusters: $[AgO_4 \cdot 3V_O^x]$ clusters for Ag1 cations, $[AgO_4 \cdot 3V_O^x]$ and $[AgO_3 \cdot 4V_O^x]$ clusters for Ag2 cations, $[AgO_4 \cdot 2V_O^x]$ clusters for Ag3 cations, and $[WO_4 \cdot 2V_O^x]$ clusters for W3 cations. Therefore, we can confirm that there is a relationship between the presence of a large amount of under-coordinated clusters at the surface and the surface energy values.[43]

A detailed analysis comparing the two different surfaces in the $\alpha$-Ag$_2$WO$_4$-R and $\alpha$-Ag$_2$WO$_4$-C morphologies, namely, the (101) and (100) exposed facets (see Figure 10), indicates that both surfaces have Ag1 and Ag2 cations at the top of each surface, but the (101) surface presents more under-coordinated $[WO_6]$ clusters near the top of the surface with respect to the (100) surface.

The natural starting point for predicting morphology type is to establish the relative stabilities of all surfaces, where the lowest surface energy will be thermodynamically preferred. While it is well-established that the kinetics required to reach different morphologies from a specific precursor state can often be manipulated by the presence of a surfactant to result in the synthesis of another morphology, the relative stability of kinetically accessible morphologies then falls within a fairly narrow range of energies. The relative stabilities of each morphology can be directly modified if they are grown in the presence of a surfactant. The surface energies of the different facets can be modified by interaction with the surfactant, which causes reordering in their relative stabilities.

Wulff's crystal representation of the optimized $\alpha$-Ag$_2$WO$_4$ is depicted in the central part of Figure 11, and the different morphologies, hexagonal rod-like $\alpha$-Ag$_2$WO$_4$-R and cuboid-like $\alpha$-Ag$_2$WO$_4$-C, can be obtained by assuming different values for the surface energies of the different facets. This interpretation has the advantage that all faces grow from the initial $\alpha$-Ag$_2$WO$_4$ crystal ($\alpha$-Ag$_2$WO$_4$−ideal), depending on their surface energy value.

From the calculated values of polyhedron energies reported in Table 2, we can obtain the energy profile that links the ideal morphology to the experimentally observed hexagonal rod-like, $\alpha$-Ag$_2$WO$_4$-R (see a Reaction Path (A) on Figure 11) and cuboid-like $\alpha$-Ag$_2$WO$_4$-C (see Reaction Path (B) on Figure 11) morphologies. Figure 11 illustrates the good agreement between the experimental and theoretical morphologies. The principal idea of this representation is that the $\alpha$-Ag$_2$WO$_4$-R and $\alpha$-Ag$_2$WO$_4$-C, associated with stable morphologies, can be energetically related to the ideal morphology along two alternative pathways via intermediates A−G.

The pathway depicted in Figure 11A involves five steps: the first one is achieved by decreasing the value of $E_{surf}$ of the (101) surface with appearance of the A morphology, followed by two stages related to an increase and decrease in the values of $E_{surf}$ for the (100) and the (001) surfaces, with formation of the B and C morphologies, respectively. The C morphology resembles the experimental $\alpha$-Ag$_2$WO$_4$-R (see Figure 4A); however, it is not elongated, as seen in Figure 4B. From C and by increasing the values of $E_{surf}$ for the (010) surface, an intermediate D morphology is reached, and by increasing the value of $E_{surf}$ for the (010) surface, the E morphology is obtained, corresponding to a maximum value of $E_{polyhedron}$. Finally, by increasing the value of $E_{surf}$ for the (110) surface, the $\alpha$-Ag$_2$WO$_4$-R morphology is achieved (see Figure 4B). Along this pathway, there is an energy barrier in the fourth step.

The pathway depicted in Figure 11B corresponds to the process linking the $\alpha$-Ag$_2$WO$_4$-C morphology and the ideal morphology. This path involves a decreasing in $E_{surf}$ values for the (100) and (001) surfaces and is a barrierless process, via E and F morphologies. This is the energetically favorable path and allows us to explain the effect of the anionic surfactant SDS in the synthesis process. As observed in the FE-SEM images in Figure 4C,D, the Ag$_2$WO$_4$-C morphology can be cubic and elongated-cubic. In this way, the four morphologies (ideal from theoretical calculations, F, G, and Ag$_2$WO$_4$-C morphologies from Figure 11B) involved in the pathway can be associated with the crystal obtained by the CP method at 90 °C with anionic surfactant SDS, since that Ag$_2$WO$_4$-C morphology is formed by the combination of (010), (100), and (001) surfaces.

The order of stability of $\alpha$-Ag$_2$WO$_4$ morphologies is $\alpha$-Ag$_2$WO$_4$-C < $\alpha$-Ag$_2$WO$_4$ ideal < $\alpha$-Ag$_2$WO$_4$-R, as shown in Figure 11. The presence of the anionic surfactant SDS in the synthesis of the $\alpha$-Ag$_2$WO$_4$ crystal prevents the formation of $\alpha$-Ag$_2$WO$_4$-R, resulting in the disappearance of (101) surface and the appearance of the (100) surface to render the $\alpha$-Ag$_2$WO$_4$-C morphology. Analysis of Figure 11B indicates that the anionic surfactant SDS interacts with and stabilizes the (100) and (001) surfaces, mainly on the Ag cations of the under-coordinated clusters. SDS also prevents increase of $E_{surf}$ of the (010) surface to form the elongated hexagonal rod-like morphology $\alpha$-Ag$_2$WO$_4$-R.

SDS has proven to be an appropriate morphology-directing agent in the CP synthesis of $\alpha$-Ag$_2$WO$_4$. This is primarily related to the surface adsorption of the anionic part of the surfactant on the different crystal surfaces, thus controlling their
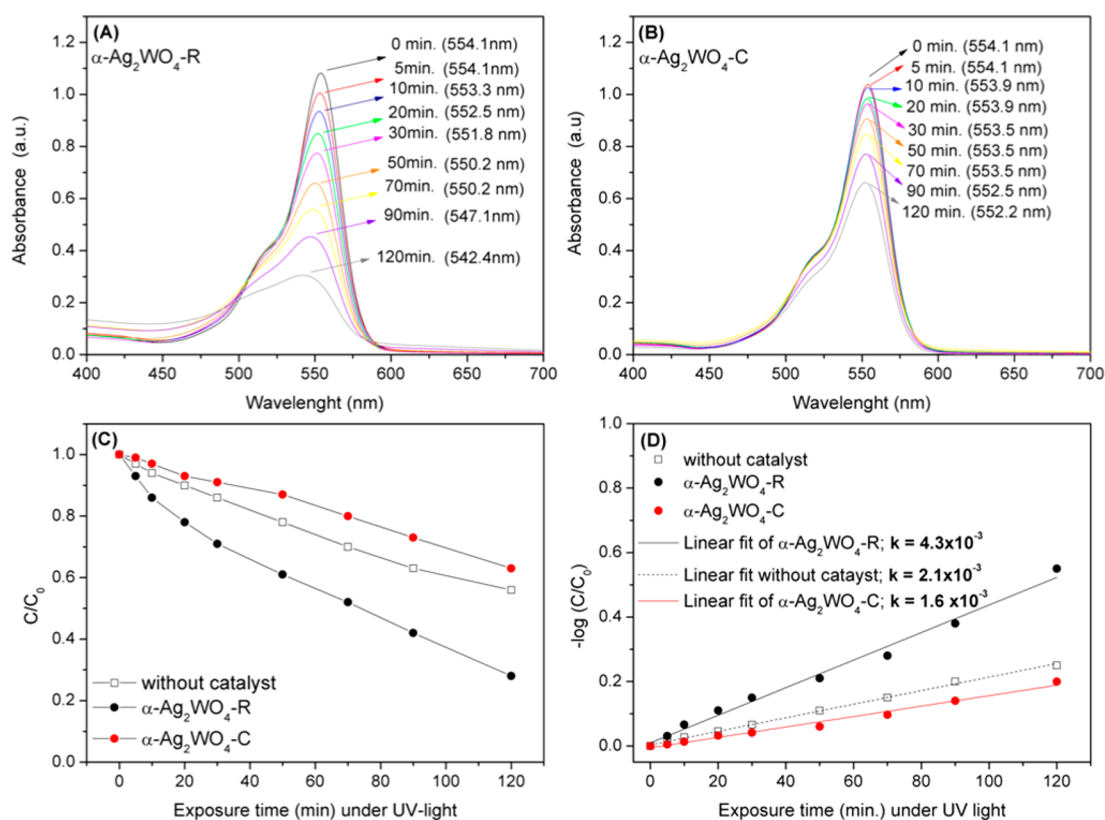
**Figure 12.** Evolution of UV−vis absorption spectra after 120 min of illumination for the degradation of RhB by the (A) $\alpha$-Ag$_2$WO$_4$-R and (B) $\alpha$-Ag$_2$WO$_4$-C crystals. (C) Photocatalysis degradation profiles of RhB with $\alpha$-Ag$_2$WO$_4$ crystals. (D) First-order kinetics of the samples.

overall morphology. This kind of adsorption is usually selective to a specific crystal plane, because the active centers of the surface are mainly associated with under-coordinated Ag cations, that is, [AgO$_n$] clusters, and consequently, such adsorption leads to an ordered morphology evolution.

**3.8. Photocatalytic Degradation.** The structural analysis of both synthesized samples of $\alpha$-Ag$_2$WO$_4$ shows that the main difference between the samples is related to surface effects. There are no significant differences in the results of XRD, FT-IR, and FT-Raman spectroscopy between both morphologies. PL analysis, however, showed significant differences in the types of defects. These experimental results, combined with the theoretical simulation of the surfaces and clusters, indicates that the behavior observed in photocatalytic reactions is due, exclusively, to morphological aspects, and a particular crystal plane enhances both the reduction/oxidation sites and the photocatalysis process.[44]

Generally, the photocatalytic process involves the following three steps: (i) the absorption of photons with energy larger than the band gap of the photocatalyst; (ii) the generation, separation, migration, or recombination of photogenerated electron−hole pairs, and (iii) the redox reactions on the photocatalyst surface. The degradation process of RhB is based on an oxidative attack by active oxygen species on an N-ethyl group. The loss of an ethyl group (N,N,N′-triethylated) at RhB has $\lambda_{max}$ = 539 nm, the loss of two ethyl groups, that results in N,N′-diethylated Rhodamine has a $\lambda_{max}$ = 522 nm, the N′-ethylated Rhodamine ($\lambda_{max}$ = 510 nm), and the de-ethylated form present at $\lambda_{max}$ = 498 nm.[45]

We monitored the degradation process by analyzing the maximum absorption bands of the RhB spectra as a function of time for both $\alpha$-Ag$_2$WO$_4$-R and $\alpha$-Ag$_2$WO$_4$-C samples. The

photocatalytic activities of the $\alpha$-Ag$_2$WO$_4$-R and $\alpha$-Ag$_2$WO$_4$-C samples are given in Figure 12A,B, respectively. The degradation of RhB UV radiation without photocatalyst or in the dark in the presence of photocatalyst is performed to understand the influence of the light or photocatalyst. The photocatalytic degradation of RhB follows pseudo-first-order kinetics, exhibiting a linear relationship between $\log(C_0/C_t)$ and the reaction time. Analysis of Figure 12A indicates a significant reduction (almost 80%) at the absorption maximum of the RhB solution after 120 min of reaction in the presence of $\alpha$-Ag$_2$WO$_4$-R as catalyst. This result correlates well with the results found in the literature for the same catalyst and conditions.[7] However, the control experiment showed that, without a photocatalyst and with $\alpha$-Ag$_2$WO$_4$-C, RhB hardly decomposed during photolysis over a period of 120 min. Analysis of Figure 12A,B indicates that RhB exhibits one band with maximum absorption at 554 nm. In addition, Figure 12A also illustrates a significant decrease in the height of the absorption maximum of RhB during the photodegradation process, while Figure 12B shows that, after 120 min, a small percentage of the dye was degraded (only 37%). This value is quite close to that of the photolysis reaction in the absence of a catalyst.

Figure 12C,D displays the linear plots of the standard kinetic data curves obtained for the RhB photodegradation process. The discoloration reaction follows first-order kinetics and can be described by the relationship $d[C]/dt = k[C]$, where $[C]$ is the RhB concentration, and $k$ indicates the overall photo-degradation rate constant and activity. By plotting $\log(C/C_0)$ as a function of time through linear regression, where $C_0$ is the initial concentration of RhB and $C$ is the concentration at time $t$, we obtained the constant $k$ (min$^{-1}$) for the photocatalysis
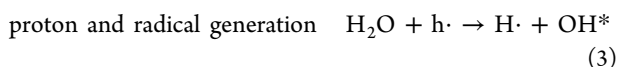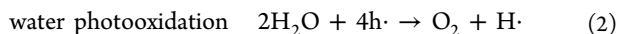
under UV–vis irradiation of each sample, from the gradients of the simulated straight lines. The corresponding values of $k$ for both $Ag_2WO_4$-R and $Ag_2WO_4$-C are $4.3 \times 10^{-3}$ min$^{-1}$ and $1.8 \times 10^{-3}$ min$^{-1}$, respectively, while the corresponding value without a catalyst is $2.1 \times 10^{-3}$ min$^{-1}$. These results point out that only the $\alpha$-$Ag_2WO_4$-R is working as a catalyst, whereas the cuboid-like morphology of $\alpha$-$Ag_2WO_4$ negatively affects the photocatalytic activity of $\alpha$-$Ag_2WO_4$. For comparison purposes, the value reported for commercial $TiO_2$ anatase (Aldrich, 99.7%), under similar experimental conditions, is $k = 2.48$ (min$^{-1}$); this is a widely applied standard for several authors.[46]

Several factors can influence reaction rate, namely, the structural defects ascribed to ordered–disordered clusters, crystallographic preferred orientation, intermediate electronic levels, high surface energy, roughness, high active surface area, facets, and so on.[47] The presence of residual anionic surfactant can also contribute to a lower photocatalytic efficiency, acting as hole scavengers.[48] However, we ensured the complete removal of surfactant, as verified by TGA (Supporting Information). According to BET data, $\alpha$-$Ag_2WO_4$ possesses a surface area of 3.72 m$^2$/g for the $\alpha$-$Ag_2WO_4$-R and only 1.22 m$^2$/g for the $\alpha$-$Ag_2WO_4$-C. The larger surface area for the $\alpha$-$Ag_2WO_4$-R in relation to $\alpha$-$Ag_2WO_4$-C is in agreement with the superior performance as photocatalyst of $\alpha$-$Ag_2WO_4$-R with respect to $\alpha$-$Ag_2WO_4$-C.

Each surface defect can act as an adsorption site for oxygen and water. The disordered $[WO_6]$ and $[AgO_n]$ clusters are located in intermediate levels near the VB, so they interact with $H_2O$ and $O_2$ molecules from the solution, by adsorption, during the photo-oxidation process. In this manner, the ordered $[WO_6]$ and $[AgO_n]$ clusters that are located below the CB can react with the $O_2$ molecules, adsorbed on the disordered clusters, by electron transference.

In the presence of air or oxygen, irradiated semiconductors can destroy many organic contaminants. The activation of $Ag_2WO_4$ by light $(h\nu)$ produces electron–hole pairs, which are powerful oxidizing and reducing agents, respectively, and the main determinant factor of catalyst efficiency is the low recombination rate between photogenerated electrons and holes on the semiconductor surface.

In the degradation of organic compounds (such as RhB), the hydroxyl radical OH*, which comes from the oxidation of adsorbed water, is the primary oxidant; and the presence of oxygen can prevent the recombination of hole–electron pairs.

$$\text{water photooxidation} \quad 2H_2O + 4h\cdot \rightarrow O_2 + H\cdot \quad (2)$$

$$\text{proton and radical generation} \quad H_2O + h\cdot \rightarrow H\cdot + OH* \quad (3)$$

As observed for the $\alpha$-$Ag_2WO_4$ semiconductor there are different $[MO_x \cdot xV_O^x]$ clusters, located on the top of the surface, and there are also $[MO_6]'_o$ polarized clusters located in the structure, where M = Ag and/or W. These clusters, in turn, can interact with $H_2O$ and $O_2$ molecules, respectively, to generate OH*, H·, and $O'_2$. The H· species are unstable and quickly interact with the superoxide radical anion ($O'_2$) forming the perhydroxyl radical ($O_2H$*). This is followed by the degradation of RhB by OH* and $O_2H$* radicals, in a cyclic process, which ends with formation of the colorless organic compounds (COC) carbon dioxide ($CO_2$) and water ($H_2O$).[49]

$$O'_2 + H\cdot \rightarrow O_2H* \quad (4)$$

$$RhB + O_2H* + OH* \rightarrow COC + CO_2 + H_2O \quad (5)$$

For the generation of all the reactive oxygen species, strong adsorption of oxygen molecule $O_2$ with concomitant electron transfer process from the oxygen vacancies[50] is necessary. In our case, both distorted $[WO_6]$ and $[AgO_n]$ clusters possess different electron density and oxygen vacancies with the capability of producing electron–hole pairs. However, thanks to the different nature of the Ag–O and W–O bonds within these clusters, the lability and the stability of these vacancies change according to the Ag/W under-coordinated clusters. The predominant presence of the surface (101) is responsible for the hexagonal rod-like morphology, $\alpha$-$Ag_2WO_4$-R, in which present under-coordinated Ag and W cations to be active for the RhB photocatalytic degradation.

Although the hexagonal rod-like morphology, $\alpha$-$Ag_2WO_4$-R, imparts a photocatalytic effect, its activity is much lower than other common catalysts, like $TiO_2$. Roca and co-workers[7] synthesized other more energetic facets of $\alpha$-$Ag_2WO_4$ by means of the microwave-assisted hydrothermal method, which is a very efficient method, but with several limitations mentioned previously. We show here that the simple use of a surfactant in a short time reaction can efficiently promote changes in morphology that directly influence the final properties of $\alpha$-$Ag_2WO_4$.

## 4. CONCLUSIONS

Good crystal facet engineering is crucial for the successful synthesis of semiconductor materials with functional applications. To develop functional materials, it is important to control their morphology and structure. The fundamental issue is a lack of in-depth knowledge about nanoparticle formation and crystallization mechanisms and about their surface chemistry. It is important to point out that the chemical environment strongly influences the growth and morphology of the crystals. Altering environmental parameters, for instance, by including surfactants, may result in modification of the surface energies of crystal faces, and consequently, the crystals obtained can present different morphologies.

The main conclusions of the present study can be summarized as follows: (i) We have experimentally obtained the cuboid-like morphology of $\alpha$-$Ag_2WO_4$-C using a simple controlled-precipitation method with the anionic surfactant SDS dissolved in a sodium tungstate solution. (ii) Although the Wulff construction, obtained by first-principles calculations, renders that the ideal morphology of $\alpha$-$Ag_2WO_4$ is the cube, this morphology is not spontaneously reached by the simple combination of those precursors in the aqueous medium. (iii) $\alpha$-$Ag_2WO_4$-C morphology is composed of the (001), (010), and (100) surfaces, and the adsorption of the SDS anionic head on the (100) facet provokes the stabilization of the (100) surface and prevents the growth process along the (101) surface. (iv) By calculating the energy profiles connecting these morphologies, a deeper insight, at atomic level, on the role of SDS surfactant is achieved, and hence, SDS has been successfully used as a morphology-controlling agent for the synthesis of $\alpha$-$Ag_2WO_4$-C. (v) The calculated energy profile, based on the Wulff construction, points out that the anionic surfactant SDS interacts with and stabilizes the (100) and (001) surfaces, mainly on the Ag cations of the under-coordinated clusters. Additionally, the SDS prevents the increase of $E_{surf}$ of the (010) surface to form the elongated hexagonal rod-like morphology $\alpha$-$Ag_2WO_4$-R. (vi) Analysis of the type and number of under-coordinated clusters of each surface suggests that on the (100) surface are mainly under-coordinated $[AgO_7]$

clusters, with a little contribution of under-coordinated $[WO_6]$ clusters, while the (101) surface is mainly formed by under-coordinated $[WO_6]$ clusters, with a minor contribution of under-coordinated $[AgO_7]$ clusters. (vii) Correlation between the exposed surfaces and photocatalytic activity was revealed, and an explanation of this behavior, arising from different morphologies and structural data, was provided. (viii) Theoretical calculations confirm the rationality of the experimental scheme and elucidate the underlying reason for the photodegradation process of Rhodamine B.

These results highlight the importance of considering the chemical environment and the adsorption of surfactant along with the synthetic route when determining the stability and activity of a catalyst with a defined morphology. Our model also reveals some details about the mechanism involved and gives some important information about how to improve photo-catalytic activity by designing the morphology of the patterned surface or improving the synthesis conditions or restructuring/shape control techniques.

Rather than individual numbers, the most important outcomes of these simulations are the general, chemical trends they have revealed. There, and here, predictive atomistic simulations are likely to play an increasingly important role. The rationally controlled chemical synthesis of well-defined morphologies may open a valuable synthetic route, and, in terms of future perspectives, this morphology control strategy can be extended to explore other Ag-based materials, where shape is the most important characteristic for application.

## ■ ASSOCIATED CONTENT

### Ⓢ Supporting Information

The Supporting Information is available free of charge on the ACS Publications website at DOI: 10.1021/acs.jpcc.8b01898.

Thermogravimetric analysis (PDF)

## ■ AUTHOR INFORMATION

### Corresponding Author

*E-mail: andres@qfa.uji.es. Phone: 0034964728083.

### ORCID Ⓘ

Amanda F. Gouveia: 0000-0003-3441-3674
Marcelo Assis: 0000-0003-0355-5565
Juan Andrés: 0000-0003-0232-3957

### Notes

The authors declare no competing financial interest.

## ■ REFERENCES

(1) Kant, R. Textile Dyeing Industry an Environmental Hazard. *Nat. Sci.* **2012**, *04*, 22−26.

(2) Mai, L.; Xu, L.; Gao, Q.; Han, C.; Hu, B.; Pi, Y. Single Beta-AgVO₃ Nanowire H₂S Sensor. *Nano Lett.* **2010**, *10*, 2604−2608.

(3) Xu, Z.; kibria, Z., Md; AlOtaibi, B.; Duchesne, P. N.; Besteiro, L. V.; Gao, Y.; Zhang, Q.; Mi, Z.; Zhang, P.; Govorov, A. O.; et al. Towards Enhancing Photocatalytic Hydrogen Generation: Which Is More Important, Alloy Synergistic Effect or Plasmonic Effect? *Appl. Catal., B* **2018**, *221*, 77−85.

(4) Teh, C. M.; Mohamed, A. R. Roles of Titanium Dioxide and Ion-Doped Titanium Dioxide on Photocatalytic Degradation of Organic Pollutants (Phenolic Compounds and Dyes) in Aqueous Solutions: A Review. *J. Alloys Compd.* **2011**, *509*, 1648−1660.

(5) Panthi, G.; Park, M.; Kim, H.-Y.; Lee, S.-Y.; Park, S.-J. Electrospun ZnO Hybrid Nanofibers for Photodegradation of Wastewater Containing Organic Dyes: A Review. *J. Ind. Eng. Chem.* **2015**, *21*, 26−35.

(6) Kumar, S. G.; Rao, K. S. R. K. Comparison of Modification Strategies Towards Enhanced Charge Carrier Separation and Photo-catalytic Degradation Activity of Metal Oxide Semiconductors (TiO₂, WO₃ and ZnO). *Appl. Surf. Sci.* **2017**, *391*, 124−148.

(7) Roca, R. A.; Sczancoski, J. C.; Nogueira, I. C.; Fabbro, M. T.; Alves, H. C.; Gracia, L.; Santos, L. P. S.; de Sousa, C. P.; Andrés, J.; Luz, G. E.; Longo, E.; et al. Facet-Dependent Photocatalytic and Antibacterial Properties of α-Ag₂WO₄ Crystals: Combining Exper-imental Data and Theoretical Insights. *Catal. Sci. Technol.* **2015**, *5*, 4091−4107.

(8) Wang, X.; Fu, C.; Wang, P.; Yu, H.; Yu, J. Hierarchically Porous Metastable Beta-Ag₂WO₄ Hollow Nanospheres: Controlled Synthesis and High Photocatalytic Activity. *Nanotechnology* **2013**, *24*, 165602.

(9) Chen, H.; Xu, Y. Photoactivity and Stability of Ag₂WO₄ for Organic Degradation in Aqueous Suspensions. *Appl. Surf. Sci.* **2014**, *319*, 319−323.

(10) van den Berg, A. J.; Juffermans, C. A. H. The Polimorphism of Silver Tungstate. *J. Appl. Crystallogr.* **1982**, *15*, 114−116.

(11) De Santana, Y. V. B.; Gomes, J. E. C.; Matos, L.; Cruvinel, G. H.; Perrin, A.; Perrin, C.; Andrès, J.; Varela, J. A.; Longo, E. Silver Molybdate and Silver Tungstate Nanocomposites with Enhanced Photoluminescence. *Nanomater. Nanotechnol.* **2014**, *4*, 22.

(12) Dutta, D. P.; Singh, A.; Ballal, A.; Tyagi, A. K. High Adsorption Capacity for Cationic Dye Removal and Antibacterial Properties of Sonochemically Synthesized Ag₂WO₄Nanorods. *Eur. J. Inorg. Chem.* **2014**, *2014*, 5724−5732.

(13) da Silva, L. F.; Catto, A. C.; Avansi, W.; Cavalcante, L. S.; Mastelaro, V. R.; Andrés, J.; Aguir, K.; Longo, E. Acetone Gas Sensor Based on α-Ag₂WO₄ Nanorods Obtained Via a Microwave-Assisted Hydrothermal Route. *J. Alloys Compd.* **2016**, *683*, 186−190.

(14) Cavalcante, L. S.; Almeida, M. A. P.; Avansi, W.; Tranquilin, R. L.; Longo, E.; Batista, N. C.; Mastelaro, V. R.; Li, M. S. Cluster Coordination and Photoluminescence Properties of α-Ag₂WO₄ Microcrystals. *Inorg. Chem.* **2012**, *51*, 10675−10687.

(15) Andrés, J.; Gracia, L.; Gonzalez-Navarrete, P.; Longo, V. M.; Avansi, W., Jr.; Volanti, D. P.; Ferrer, M. M.; Lemos, P. S.; La Porta, F. A.; Hernandes, A. C.; et al. Structural and Electronic Analysis of the Atomic Scale Nucleation of Ag on Alpha-Ag₂WO₄ Induced by Electron Irradiation. *Sci. Rep.* **2015**, *4*, No. 5391(7pp), DOI: 10.1038/srep05391.

(16) Derby, J. J.; Atherton, L. J.; Gresho, P. M. An Integrated Process Model for the Growth of Oxide Crystals by the Czochralski Method. *J. Cryst. Growth* **1989**, *97*, 792−826.

(17) Cui, X.; Yu, S. H.; Li, L.; Biao, L.; Li, H.; Mo, M.; Liu, X. M. Selective Synthesis and Characterization of Single-Crystal Silver Molybdate/Tungstate Nanowires by a Hydrothermal Process. *Chem. - Eur. J.* **2004**, *10* (1), 218−223.

(18) Nguyen, N. T.; Nguyen, B. H.; Ba, D. T.; Pham, D. G.; Van Khai, T.; Nguyen, L. T.; Tran, L. D. Microwave-Assisted Synthesis of Silver Nanoparticles Using Chitosan: A Novel Approach. *Mater. Manuf. Processes* **2014**, *29* (4), 418−421.

(19) George, T.; Joseph, S.; Mathew, S. Synthesis and Characterization of Nanophased Silver Tungstate. *Pramana* **2005**, *65* (5), 793–799.

(20) Niu, Z.; Li, Y. Removal and Utilization of Capping Agents in Nanocatalysis. *Chem. Mater.* **2014**, *26*, 72–83.

(21) Deshmukh, R.; Niederberger, M. Mechanistic Aspects in the Formation, Growth and Surface Functionalization of Metal Oxide Nanoparticles in Organic Solvents. *Chem. - Eur. J.* **2017**, *23*, 8542–8570.

(22) Bakshi, M. S. How Surfactants Control Crystal Growth of Nanomaterials. *Cryst. Growth Des.* **2016**, *16*, 1104–1133.

(23) Brunauer, S.; Teller, E.; Emmett, P. H. Adsorption of Gases in Multimolecuar Layers. *J. Am. Chem. Soc.* **1938**, *60*, 309–319.

(24) Andrés, J.; Gracia, L.; Gouveia, A. F.; Ferrer, M. M.; Longo, E. Effects of Surface Stability on the Morphological Transformation of Metals and Metal Oxides as Investigated by First-Principles Calculations. *Nanotechnology* **2015**, *26*, 405703.

(25) Ferrer, M. M.; Gouveia, A. F.; Gracia, L.; Longo, E.; Andrés, J. A 3D Platform for the Morphology Modulation of Materials: First Principles Calculations on the Thermodynamic Stability and Surface Structure of Metal Oxides: $Co_3O_4, \alpha$-$Fe_2O_3$, and $In_2O_3$. *Model.Simul. Mater. Sci. Eng.* **2016**, *24*, No. 025007(10pp), DOI: 10.1088/0965-0393/24/2/025007.

(26) Skarstad, P. M.; Geller, S. $(W_4O_{16})^{8-}$ Polyion in the high temperature modification of silver tungstate. *Mater. Res. Bull.* **1975**, *10*, 791–799.

(27) Rietveld, H. M. A. Profile Refinement Method for Nuclear and Magnetic Structures. *J. Appl. Crystallogr.* **1969**, *2*, 65–71.

(28) Longo, V. M.; de Foggi, C. C.; Ferrer, M. M.; Gouveia, A. F.; André, R. S.; Avansi, W.; Vergani, C. E.; Machado, A. L.; Andrés, J.; Cavalcante, L. S.; et al. Potentiated Electron Transference in Alpha-$Ag_2WO_4$ Microcrystals with Ag Nanofilaments as Microbial Agent. *J. Phys. Chem. A* **2014**, *118*, 5769–78.

(29) Longo, E.; Cavalcante, L. S.; Volanti, D. P.; Gouveia, A. F.; Longo, V. M.; Varela, J. A.; Orlandi, M. O.; Andres, J. Direct in Situ Observation of the Electron-Driven Synthesis of Ag Filaments on Alpha-$Ag_2WO_4$ Crystals. *Sci. Rep.* **2013**, *3*, 1676.

(30) Longo, E.; Avansi, W., Jr.; Bettini, J.; Andres, J.; Gracia, L. *In Situ* Transmission Electron Microscopy Observation of Ag Nanocrystal Evolution by Surfactant Free Electron-Driven Synthesis. *Sci. Rep.* **2016**, *6*, 21498.

(31) Clark, G. M.; Doyle, W. P. Infra-Red Spectra of Anhydrous Molybdates and Tungstates. *Spectrochim. Acta* **1966**, *22*, 1441–1447.

(32) Turkovic, A.; Fox, D. L.; Scott, J. F.; Geller, S.; Ruse, G. F. High Temperature Raman Spectroscopy of Silver Tetratungstate, $Ag_8W_4O_{16}$. *Mater. Res. Bull.* **1977**, *12*, 189–195.

(33) Wood, D. L.; Tauc, J. Weak Absorption Tails in Amorphous Semiconductors. *Phys. Rev. B* **1972**, *5*, 3144–3151.

(34) Kubelka, P.; Munk, F. Ein Beitrag zur Optik der Farbanstriche. *Z. Techn. Phys.* **1931**, *12*, 593–601.

(35) Kim, D. W.; Cho, I.-S.; Lee, S.; Bae, S.-T.; Shin, S. S.; Han, G. S.; Jung, H. S.; Hong, K. S. Photophysical and Photocatalytic Properties of $Ag_2M_2O_7$ (M = Mo, W). *J. Am. Ceram. Soc.* **2010**, *93*, 3867–3872.

(36) Tang, J.; Ye, J. Correlation of Crystal Structures and Electronic Structures and Photocatalytic Properties of the W-Containing Oxides. *J. Mater. Chem.* **2005**, *15*, 4246.

(37) Sczancoski, J. C.; Cavalcante, L. S.; Joya, M. R.; Varela, J. A.; Pizani, P. S.; Longo, E. $SrMoO_4$ Powders Processed in Microwave-Hydrothermal: Synthesis, Characterization and Optical Properties. *Chem. Eng. J.* **2008**, *140*, 632–637.

(38) Lin, Z.; Li, J.; Zheng, Z.; Yan, J.; Liu, P.; Wang, C.; Yang, G. W. Electronic Reconstruction of $Ag_2WO_4$ Nanorods for the Visible-Light Photocataysis. *ACS Nano* **2015**, *9*, 7256–7265.

(39) Longo, E.; Volanti, D. P.; Longo, V. M.; Gracia, L.; Nogueira, I. C.; Almeida, M. A. P.; Pinheiro, A. N.; Ferrer, M. M.; Cavalcante, L. S.; Andrés, J. Toward an Understanding of the Growth of Ag Filaments on $\alpha$-$Ag_2WO_4$ and Their Photoluminescent Properties: A Combined Experimental and Theoretical Study. *J. Phys. Chem. C* **2014**, *118*, 1229–1239.

(40) Martin, D. J.; Liu, G.; Moniz, S. J.; Bi, Y.; Beale, A. M.; Ye, J.; Tang, J. Efficient Visible Driven Photocatalyst, Silver Phosphate: Performance, Understanding and Perspective. *Chem. Soc. Rev.* **2015**, *44*, 7808–28.

(41) Huang, K.; Yuan, L.; Feng, S. Crystal Facet Tailoring Arts in Perovskite Oxides. *Inorg. Chem. Front.* **2015**, *2*, 965–981.

(42) Kröger, F. A.; Vink, H. J. Relations Between the Concentrations of Imperfections in Crystalline. *Solid State Phys.* **1956**, *3*, 307–435.

(43) Liu, G.; Yu, J. C.; Lu, G. Q.; Cheng, H. M. Crystal Facet Engineering of Semiconductor Photocatalysts: Motivations, Advances and Unique Properties. *Chem. Commun.* **2011**, *47*, 6763–83.

(44) Huang, M.; Weng, S.; Wang, B.; Hu, J.; Fu, X.; Liu, P. Various Facet Tunable ZnO Crystals by a Scalable Solvothermal Synthesis and Their Facet-Dependent Photocatalytic Activities. *J. Phys. Chem. C* **2014**, *118*, 25434–25440.

(45) Wu, T. L. G.; Zhao, J.; et al. Photoassisted Degradation of Dye Pollutants. V. Self-Photosensitized Oxidative Transformation of Rhodamine B Under Visible Light Irradiation in Aqueous $TiO_2$ Dispersions. *J. Phys. Chem. B* **1998**, *102*, 5845–5851.

(46) Akpan, U. G.; Hameed, B. H. Parameters Affecting the Photocatalytic Degradation of Dyes Using $TiO_2$-based Photocatalysts: A Review. *J. Hazard. Mater.* **2009**, *170*, 520–529.

(47) Cavalcante, L. S.; Sczancoski, J. C.; Batista, N. C.; Longo, E.; Varela, J. A.; Orlandi, M. O. Growth Mechanism and Photocatalytic Properties of $SrWO_4$ Microcrystals Synthesized by Injection of Ions into a Hot Aqueous Solution. *Adv. Powder Technol.* **2013**, *24*, 344–353.

(48) Horváth, O.; Bodnár, E.; Hegyi, J. Photoassisted Oxidative Degradation of Surfactants and Simultaneous Reduction of Metals in Titanium Dioxide Dispersions. *Colloids Surf., A* **2005**, *265*, 135–140.

(49) Bomio, M. R. D.; Tranquilin, R. L.; Motta, F. V.; Paskocimas, C. A.; Nascimento, R. M.; Gracia, L.; Andres, J.; Longo, E. Toward Understanding the Photocatalytic Activity of $PbMoO_4$ Powders with Predominant (111), (100), (011), and (110) Facets. A Combined Experimental and Theoretical Study. *J. Phys. Chem. C* **2013**, *117*, 21382–21395.

(50) Plantard, G.; Janin, T.; Goetz, V.; Brosillon, S. Solar Photocatalysis Treatment of Phytosanitary Refuses: Efficiency of Industrial Photocatalysts. *Appl. Catal., B* **2012**, *115–116*, 38–44.